This is the post-print version of the following article: Andrés-Sanz, D; Diamanti, E; Di Silvo, D; Gurauskis, J; López-Gallego, F. Selective Coimmobilization of His-Tagged Enzymes on Yttrium-Stabilized Zirconia-Based Membranes for Continuous Asymmetric Bioreductions. ACS Appl. Mater. Interfaces 2022, 14, 3, 4285–4296

DOI: 10.1021/acsami.1c20738

Selective co-immobilization of His-tagged enzymes on Yttrium-Stabilized Zirconia based membranes for continuous asymmetric bioreductions

Daniel Andrés-Sanz [a], Eleftheria Diamanti [a], Desirè Di Silvo [a], Jonas Gurauskis *[b,c], and Fernando López-Gallego*[a,d]

a. Center for Cooperative Research in Biomaterials (CIC biomaGUNE), Basque Research and Technology Alliance (BRTA), Paseo de Miramón 182 20014, Donostia-San Sebastián, Spain

b. INMA, Aragón Nanoscience and Materials Institute (CSIC-Unizar), Calle Mariano Esquillor 15, Edificio CIRCE, 50018 Zaragoza, Spain.

c. ARAID, Aragonese Agency for Research and Development, Av. de Ranillas 1-D, planta 2ª, Oficina B, 50018 Zaragoza, Spain.

d. IKERBASQUE, Basque Foundation for Science, María Díaz de Haro 3, 48013 Bilbao, Spain

***Corresponding authors**

Fernando López-Gallego: flopez@cicbiomagune.es

Jonas Gurauskis: jonas.gurauskis@csic.es

Abstract

Scalability, process control, and modularity are some of the advantages that make flow biocatalysis a key enabling technology for green and sustainable chemistry. In this context, rigid porous solid membranes hold the promise to expand the toolbox of flow-biocatalysis due to their chemical stability and inertness. Yttrium-stabilized zirconia (YSZ) fulfills these properties, however, it has been scarcely exploited as a carrier for enzymes. Here, we discovered an unprecedented interaction between YSZ materials and His-tagged enzymes that enables the fabrication of multi-functional biocatalytic membranes for bioredox cascades. X-photon electron spectroscopy suggests that enzyme immobilization is driven by coordination interactions between the imidazole groups of His-tags and both Zr and Y atoms. As model enzymes, we co-immobilized in-flow a thermophilic hydroxybutyryl-CoA dehydrogenase (TtHBDH-His) and a formate dehydrogenase (His-CbFDH) for the continuous asymmetric reduction of ethyl acetoacetate with *in situ* redox cofactor recycling. Fluorescence confocal microcopy deciphered the spatial organization of the two co-immobilized enzymes, pointing out the importance of the co-immobilization sequence. Finally, the co-immobilized system succeeded in *situ* recycling the redox cofactor maintaining the specific productivity using only 0.05 mM NADH and accumulating a total enzyme turnover number of 4000 in 24 h. This work presents YSZ materials as ready-to-use carriers for the site-directed enzyme in-flow immobilization and the application of the resulting heterogeneous biocatalysts for continuous biomanufacturing.

Keywords: Flow biocatalysis, protein immobilization, inorganic membranes, YSZ, multi-enzyme system

INTRODUCTION

In the last decade, biocatalysis and flow chemistry has met to intensify a myriad of synthetic processes from bulk synthesis to fine chemistry.[1-3] Enzymatic reactions in flow, or what is more recently dubbed as flow-biocatalysis, emerge as an alternative to traditional batch processes to further intensify biotransformations, boosting their reaction productivity and favoring their scale-up and work-up.[4] For all these reasons, flow biocatalysis has become a reference in green and sustainable chemistry.[2, 3, 5] The vast majority of enzymatic reactions in flow involve immobilized biocatalysts as they are easily integrated into a diversity of plug-flow reactor designs and effortlessly replaced once the enzymes are inactive upon their operational use. The successful completion of this transition requires parallel breakthroughs in diverse fields from biocatalyst development to reactor design. Here, material sciences have enormously contributed to the advance of flow-biocatalysis through synthesizing new solid carriers and surfaces that immobilize enzymes with high activity and stability retention. To that end, material architecture and surface functionality have been engineered to optimize the interfaces between the enzyme and the carrier, and between the biocatalytic material and the reactor configuration.[6]

Although macroporous membranes have been mainly exploited for chromatographic bioseparation and proteomics,[7] flow-biocatalysis has also harnessed these architectures as an alternative to packed-bed reactors (PBRs). This is mainly because membranes present a suitable porosity to immobilize enzymes and operate them through convective flow dynamics that allow an efficient mass transfer.[8] In particular, inorganic membranes formed by solid oxides or carbides exhibit excellent thermal, chemical, and mechanical endurance in long operational runs.[9] For enzyme immobilization purposes, the most studied inorganic materials are alumina, silica, titania and to a lesser extent yttria-stabilized zirconia (YSZ)[10-12]. In particular, YSZ delivers one of the highest toughness found in solid oxide materials due to its inherent martensitic transformation toughening which makes it highly resistant to crack propagation.[13, 14] In fact, this material has been denoted as “ceramic steel”. YSZ’s mechanical stability in combination with its high chemical resistivity, wear resistance, tailored hierarchical porosity, and biocompatibility make it an excellent material as a carrier for enzyme immobilization. However, direct immobilization of enzymes on the surface of these inorganic membranes is often challenging due to their inert nature. Consequently, the

physical adsorption of enzymes on the surface of plain inorganic membranes often result in heterogeneous biocatalysts with low enzyme loads for practical purposes.[15] Hence, upon conformation and sintering, most inorganic membranes need to be functionalized with organic molecules to efficiently immobilize enzymes. A vast chemical diversity is available for activating inorganic materials, however, the use of 3-aminopropyltriethoxysilane (APTES) and glutaraldehyde dominate functionalization strategies over using other reactive groups such epoxides or alkenes.[11] These immobilization chemistries immobilize proteins randomly, controlling poorly their orientation unless the protein surface is engineered.[16-18] To advance in site-selective immobilization of enzymes across the porous inorganic membrane surfaces, these materials can be functionalized with metal chelates (i.e., Ni-NTA) that selectively immobilize His-tagged enzymes through affinity interactions.[19] Unfortunately, the functionalization of inorganic membranes with organic reactive groups is precluded during the fabrication process (high-temperature sintering conditions), and thus post-manufacturing functionalization is required. However, membrane functionalization upon manufacturing does not assure uniform coverage of the reactive groups across the membrane surface.

As an alternative to membrane functionalization with organic elements, inorganic reactive elements can be *in situ* added during the membrane manufacturing to further enable the enzyme anchoring.[20] Precipitated metal hydroxides have been sintered with solid oxides to form composites able to immobilize enzymes yet in a random manner.[21, 22] Inorganic membranes have also been functionalized with metal oxide nanoparticles during their fabrication process. This latter strategy has been exploited for supporting inorganic nanocatalysts,[23] but rarely intended for site-selective enzyme immobilization,[24] despite some nanoparticles (i.e., Nickel Oxide (NiO) nanoparticles) have shown a high affinity towards His-tagged proteins.[24, 25]

In this work, we report the preparation of naked YSZ porous membranes and their further functionalization with NiO nanoparticles (NiOnp). The sintered disk-shaped YSZ membranes were evaluated for the site-selective co-immobilization of His-tagged industrially relevant enzymes. Beyond the glucose oxidase/peroxidase system exhaustively used in material engineering for glucose detection,[26] we select the NADH-dependent and His-tagged 3-hydroxybutyryl-CoA dehydrogenase from *Thermus thermophilus* HB27 (TtHBDH-His) and a formate dehydrogenase from *Candida boidinii* (His-CbFDH) as a bi-enzyme model system (Figure 1).[27, 28] We found that these two His-

tagged enzymes were selectively immobilized on naked YSZ membranes without requiring the surface activation with NiO nanoparticles. Finally, we studied the effect of flow rate and cofactor concentration on the overall specific productivity of the co-immobilized multi-enzyme system for the continuous asymmetric reduction of β-ketoesters with *in situ* NADH recycling.[27]

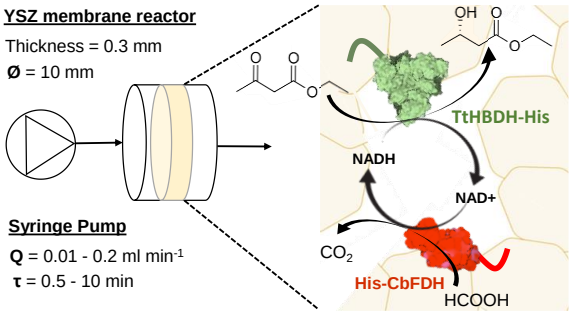

Figure 1: Scheme of the flow reactor set up for the continuous asymmetric reduction of β-ketoesters with *in-situ* cofactor recycling catalyzed by the TtHBDH-His and His-CbFDH co-immobilized on YSZ membranes.

RESULTS AND DISCUSSION

YSZ based membrane fabrication and characterization

Figure 2 shows the SEM backscattered images that illustrate the main steps of the synthesis of the YSZ based membranes herein fabricated according to a protocol described elsewhere.[29]

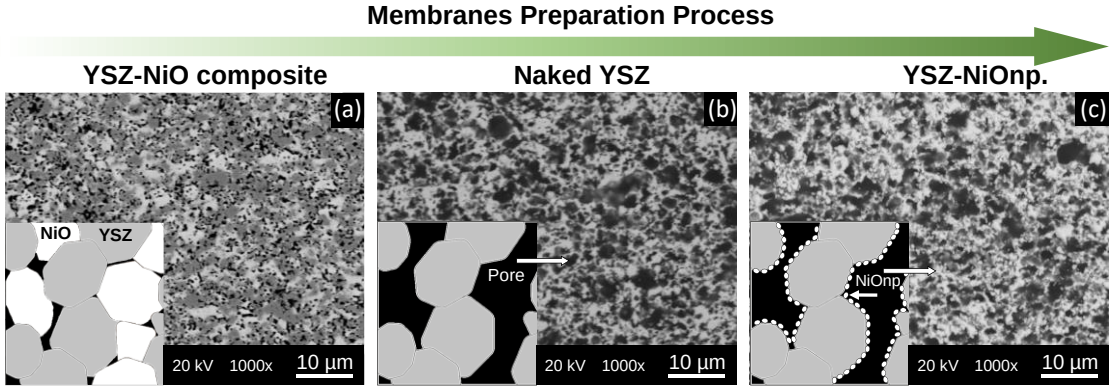

Figure 2. SEM micrographs and schematic representation of YSZ based membrane microstructure evolution through its preparation. The black holes within SEM images correspond to the microstructural porosity. (a) SEM micrograph of sintered YSZ-NiO composite. (b) naked YSZ membrane after acid leaching of Ni phase (c) SEM micrograph after the 4 infiltration cycles of naked YSZ membrane with NiO nanoparticles followed

by a thermal treatment. The inlets in the bottom left corner of all SEM micrographs depict the fabrication process where YSZ, NiO, and porous phases appear as light gray, white, and black respectively.

First, we sintered YSZ–NiO composites (Figure 2a) which present evenly distributed YSZ and NiO phases with relatively low structural porosity (15%) as detected by mercury intrusion porosimetry (Figure S1). After NiO reduction and leaching of Ni metallic phase, highly porous YSZ membranes were achieved (Figure 2b). Complete elimination of the Ni phase resulted in naked YSZ membranes with 60% porosity and the presence of macropores (> 0.5 μm) (Table 1, Figure S1). Despite such relatively high porosity, the manipulation of ~300 μm thin naked YSZ membranes was possible due to their high structural robustness and interconnectivity of the YSZ phase. The naked YSZ membranes were then functionalized with nickel oxide nanoparticles (NiOnp) of 5-7 nm through step-wise vacuum infiltration and thermal treatment. We performed up to 4 consecutive infiltration cycles to increase YSZ functionality with NiO (Figure 2c). As expected, high magnification SEM images showed the presence of NiO nanoparticles at the walls of the YSZ porous scaffolds (Figure S2). EDX analysis of YSZ membranes confirmed the co-localization of Zr, Y, and Ni atom (Figure S3).

Initial observation through SEM images (Figure 2c) show that the macropores range of YSZ based membranes appeared almost unaltered even after 4 infiltration cycles. Nevertheless, the specific surface area, the overall porosity, and pore size distribution are slightly modified upon the consecutive infiltration cycles (see Table 1 and Figure S1). Surface area values were doubled after the first infiltration cycle as expected, and then it was slightly reduced with consecutive infiltration cycles mainly due to the microstructural porosity/void filling effect. Hence, a highly porous and permeable network of YSZ membranes (either naked or NiOnp functionalized) with porosity values above 50% were achieved. Depending on the number of infiltration cycles, we named the resulting YSZ membranes as YSZ-NiOnp x1, YSZ-NiOnp x2, and YSZ-NiOnp x4 for one, two, and four cycles, respectively.

In-flow immobilization of His-tagged enzymes on YSZ based membrane reactors

We evaluated different YSZ materials (naked YSZ and YSZ-NiOnp x1-4) as supports for the immobilization of a thermophilic NADH dependent hydroxybutyryl-CoA dehydrogenase tagged with a poly-His at its C-terminus (TtHBDH-His). This enzyme has

been proven to be very efficient for the asymmetric reduction of β-ketoesters[27] to yield the corresponding enantiopure (*S*)-β-hydroxy esters. For all YSZ materials, we prepared membrane reactors with a circular shape of 20 mm diameter and 0,3 mm thickness into a polycarbonate filter holder. Next, we flushed 1 mg of TtHBDH-His through the membrane reactor. First, we determined the enzyme load upon the in-flow immobilization through measuring the enzyme concentration in the outlet of the flow reactor and then calculating the mass balance regarding the inlet enzyme concentration (Table 1).

Table 1. Enzyme load and activities with different YSZ supports.

		YSZ	YSZ-NiOnp x1	YSZ-NiOnp x2	YSZ-NiOnp x4
Membrane weight	(g)	0.20	0.28	0.31	0.38
Specific area	(m^2 x g^{-1})	2.02	4.20	3.73	3.39
Porosity	(%)	60	57	56	51
Load per weight [(a)]	(mg × g^{-1})	4.10	0.79	0.71	0.68
Load per surface	(mg × m^{-2})	2.031	0.190	0.191	0.201
Specific immobilized activity [(b)]	(U × mg^{-1})	0.095 ± 0.007	0.111 ± 0.021	0.098 ± 0.012	0.031 ± 0.004
Relative recovered activity [(c)]	(%)	67 ± 1	80 ± 12	71 ± 15	23 ± 9
Surface activity	(U × m^{-2})	0.190	0.020	0.019	0.006

(a): 1 mL of 1mg × mL^{-1} enzyme solution was flushed through the membrane (inlet concentration) (**b):** Activity experiments were carried out with membranes in which 0.1mg TtHBDH-His was immobilized. The reaction flow rate was 0.2 mL × min^{-1} **(c)**: Relative recovered activity = (Recovered specific activity of immobilized enzyme / Specific activity of soluble enzyme). The activity of soluble enzyme: 0.14 U × mg^{-1}.

When we assessed the immobilization of TtHBDH-His on naked YSZ membranes, we found that such material loaded 4 and 10 times more protein per mass and surface of the material, respectively than those infiltrated with NiO nanoparticles (Table 1). Despite lacking the nickel atoms that favor the enzyme immobilization through the His-tag and exhibiting a smaller specific area, the YSZ scaffold is also able to load a larger amount of protein per surface than YSZ-NiOnp x1-4 membranes. Furthermore, the high protein load exhibited by naked YSZ breaks the trend that a higher surface area loads more protein per mass of material. This result indicates that the infiltration of NiO nanoparticles provides the material with a larger specific surface area which might be

ineffective for the enzyme immobilization. We suggest that the newly created pores within mesoporous range (< 100 nm) by the nanometric NiO phase are too small to be colonized by large macromolecules like TtHBDH-His (Mw:192 kDa) (see Figure S1). Therefore, the extra surface created by the nanoparticle infiltration seems to be inefficient and underutilized for the immobilization of relatively large enzymes.

Besides the protein loading, we also analyzed the activity of TtHBDH-His immobilized on the different membranes loaded with 0.1 mg of enzyme. To that aim, we determined the conversion of NADH by measuring spectrophotometrically the remaining concentration of NADH at the outlet of the flow-reactor operated at 0.2 mL × min^{-1}. In the continuous activity assay of TtHBDH-His immobilized on YSZ-NiOnp (x1, x2, x4) membranes, we found an inverse correlation between the amount of infiltrated nanoparticles and the recovered specific activity. This drop was dramatic for YSZ-NiOnp x4 where the recovered specific activity of TtHBDH-His was only 23% of that measured for the soluble enzyme (Table 1), resulting in an immobilized biocatalyst with the lowest surface activity (0.006 U × m^{-2}) of those herein tested. This data suggests that the high density of NiO nanoparticles may establish surface-enzyme contacts that drive detrimental structural rearrangements on the enzyme functionality. [30]

When a naked YSZ membrane was used as the carrier, the immobilized TtHBDH-His exhibited 67% of the free enzyme specific activity but presented the highest surface activity (0.190 U × m^{-2}) herein reported. Hence, the naked YSZ membrane loads up to 10 times more protein and exhibits 10-fold highest surface activity than the YSZ scaffolds functionalized with NiOnp. All in all, these results suggest that the YSZ surface plays a major role in binding His-tagged enzymes. When YSZ dominates the immobilization process over the NiO nanoparticles, both enzyme loading and recovered activity increase. As the immobilization mechanism of TtHBDH-His on naked YSZ remains unknown but this immobilization protocol shows excellent results, we further investigate the immobilization process and optimize the continuous biocatalytic reaction using naked YSZ.

Understanding the immobilization chemistry of His-tagged enzymes on naked YSZ membranes

Intrigued by the unexpected immobilization of TtHBDH-His on naked YSZ membranes, we interrogated which protein residues drive the immobilization. First, we analyzed the role of the His-tag in the immobilization chemistry. To that end, we constructed an untagged variant of TtHBDH and tested its immobilization on naked YSZ

under the same conditions used for TtHBDH-His. Table 2 shows the protein loadings of both His-tagged and untagged enzymes immobilized under different conditions. In the absence of His-tag, the protein load was only 15% of the offered enzyme compared to the 82% achieved with its His-tagged counterpart. This insight points out the main role of His-tag during the immobilization process although the interaction of such polypeptide with the YSZ surface remains elusive. Proteins are known to be immobilized on YSZ surface through electrostatic interactions,[31] but His-tag driven immobilization has never been reported on this type of materials to the best of our knowledge.

Table 2. Enzyme immobilization of non-tagged and His-tagged enzyme on YSZ

		TtHBDH	**TtHBDH-His**		
		(Buffer)	(Buffer)	(1M NaCl)	(1M Imidazole)
Max. Load [(a)]	(mg enzyme × membrane^{-1})	0.15	0.82	0.43	0.05
Load per weight [(b)]	(mg enzyme × g^{-1})	0.75	4.1	2.1	0.25
Load per surface [(c)]	(mg enzyme × m^{-2})	0.37	2.03	1.06	0.12

(a) Maximum load offering 1 mg of enzyme per membrane (b) YSZ membrane weight: 0.2 g
(c) Specific area of YSZ: 2.02 m^{2} × g^{-1}

To decipher the nature of the interactions that drive the protein immobilization on YSZ, we immobilized in-flow TtHBDH-His on YSZ disks in presence of 1M NaCl to avoid electrostatic interactions (1M NaCl), and with 1 M imidazole to preclude the histidine coordination chemistry with Y and Zr atoms at the membrane surface (Table 2). The samples collected from the outlet of the reactor were analyzed by Bradford assay. We observed that the high ionic strength reduced the immobilization yield to 50%, whereas the immobilization was almost abolished (6% immobilization yield) in presence of imidazole. Furthermore, the proteins bound to those membranes were desorbed through flushing with 1M NaCl and 1M imidazole. The eluted protein fractions recovered from the reactor outlet were analyzed by SDS-PAGE (Figure S4), confirming the results obtained with the Bradford assay (Table 2). This set of experiments demonstrates that the untagged enzyme was only eluted with high salt concentration, while the His-tagged enzyme was fully released with 1M imidazole (Figure S4a-b). In those materials where electrostatic interactions were avoided during the immobilization process, proteins were

only eluted with imidazole (Figure S4c-d). These data reveal that the immobilization chemistry of His-tagged enzymes on naked YSZ involves a complex mechanism dominated by the metal-coordination between His-tag and the YSZ surface but also favored by electrostatic interactions between the protein surface and the YSZ scaffold. Remarkably, when we incubated naked YSZ with a crude extract containing TtHBDH-His, we demonstrated that the His-tagged enzyme was preferentially bound to this material, allowing the protein purification upon imidazole elution (Figure S5). Hence, YSZ materials enable the one-step purification/immobilization of His-tagged enzymes similarly to the previously described controlled porosity glass (CPG) particles functionalized with cobalt (II) complexes. [32]

Once we evidenced the key role of His-tag for the protein immobilization on naked YSZ materials, we further characterized the enzyme-YSZ interactions through X-ray photoelectron spectroscopy analysis (XPS) to understand the contribution of Yttrium and Zirconium to the enzyme binding.[33] To gain resolution in the XPS measurements, we performed the immobilization of untagged TtHBDH and TtHBDH-His on non-porous YSZ surfaces. XPS spectra, allowed us to determine the relative chemical composition of the samples (Table S1). A larger percentage of carbon and the detection of nitrogen confirm the presence of proteins on the surface of YSZ. Moreover, the atomic ratio (Zr+Y)/N was 3 times smaller for the His-tagged enzyme than for its untagged counterpart (Table S2), supporting the essential role of the His-tag in the immobilization mechanism. Figure 3 illustrates the changes in N 1s, Zr 3d, and Y 3d regions of XPS spectra when TtHBDH-His is bound to naked YSZ (YSZ@TtHBDH-His) compared to YSZ just incubated with the immobilization buffer (25 mM sodium phosphate, pH 7). The analysis of N1s signal (Figure 3a and Figure S6) and the relative peak fitting confirms the presence of organic nitrogen species (-N=; -N-; NH+) corresponding to protein amino acids, including histidines. [34-36]

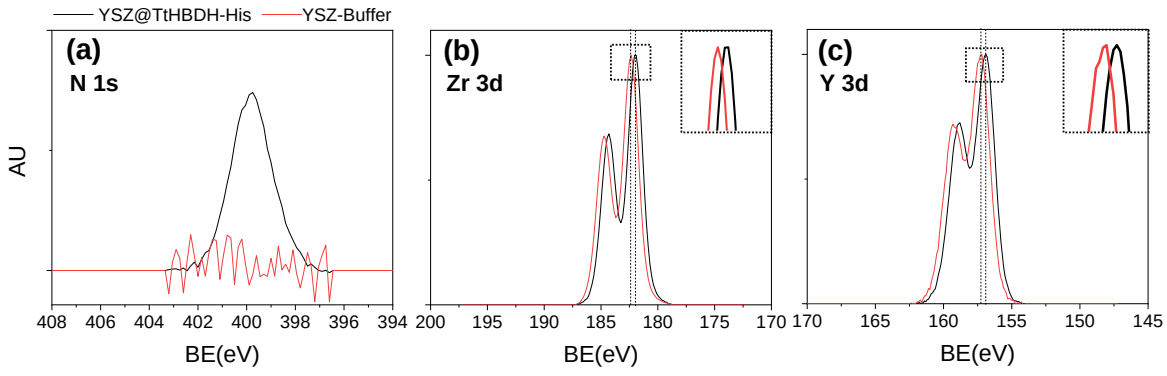

Figure 3: X-ray photoelectron spectra of non-porous YSZ (black) and YSZ@TtHBDH-His (red) surfaces. (a): Nitrogen 1s spectra, (b) Zirconium 3d spectrum and (c) Yttrium 3d spectrum. The inlet of B and C correspond to the black dashed squares to better visualize the peak shift of Zr and Y when the enzyme is immobilized.

In both YSZ and YSZ@TtHBDH-His, we detected two peaks $3d_{5/2}$ and $3d_{3/2}$ at 184.8 and 182.4 eV corresponding to the signals of Zr 3d orbitals (Figure 3b and Figure S7).[34, 36] Likewise, the signal of Y 3d orbitals appeared as two peaks at 159.4 eV (Y $3d_{5/2}$) and 157.2 eV (Y $3d_{3/2}$) (Figure 3c and Figure S8). Zr and Y 3d signals are associated with Zr^{4+} and Y^{3+} states respectively, which are linked to its corresponding oxides (Figure S9).[37] Remarkably, the Zr and Y 3d peaks of the YSZ@TtHBDH-His sample are slightly shifted towards lower binding energies (Figure 3b-c), indicating significant changes in the chemical environment of Zr and Y when the protein is bound to YSZ. Jeon et al. reported a similar shift in Mo 3d orbital of Molybdophosphoric acid when bound to imidazole.[38] Hence, we suggest that the imidazole rings of the Histidine-tag can coordinate both Y and Zr displayed at the surface of the YSZ, enabling the enzyme immobilization. Both the presence of nitrogen and the shifts of Zr and Y were also observed in the XPS spectra of YSZ@TtHBDH-His using the porous materials that will be implemented as heterogeneous biocatalysts for further process developments.

The XPS together with the mass balance of the immobilization process using both tagged and untagged enzymes demonstrate that the His-tag drives the enzyme immobilization on YSZ without requiring other directing groups such as nickel oxides as occurs with other porous materials such as cellulose[25] or silica[39]. As far as we know, this is the first evidence of the direct and selective immobilization of His-tagged enzymes on non-functionalized YSZ porous materials.

Co-immobilization and spatial distribution of His-tagged enzymes on naked YSZ

Once we proved the site-directed immobilization of TtHBDH-His on naked YSZ and the excellent functional properties of such immobilized system for the asymmetric reduction of ethyl acetoacetate (EAA), we expanded this method to other His-tagged proteins. Formate dehydrogenase from *Candida bodiini* tagged with a His-tag in its N-terminus (His-CbFDH) was immobilized on YSZ membranes as a redox partner for TtHBDH-His, achieving a 100% immobilization yield with a loading of 0.5 mg_{HisFDH} x g_{YSZ}^{-1}. Furthermore, we first immobilized TtHBDH-His labeled with FITC (Fluorescein isothiocyanate) followed by the immobilization of His-CbFDH labelled with Rhodamine

B (RhB) on the same naked YSZ membrane and studied their enzyme spatial organization through confocal laser scanning microscopy (CLSM). The resulting images were analyzed to provide both qualitative and quantitative data about the enzyme co-localization on the YSZ scaffold. CLSM images show that both enzymes are distributed over the entire surface (Figure 4a-c). Although the Manders coefficient (Table S3) revealed that 95% of TtHBDH-His co-localizes with His-CbFDH in the analyzed region,

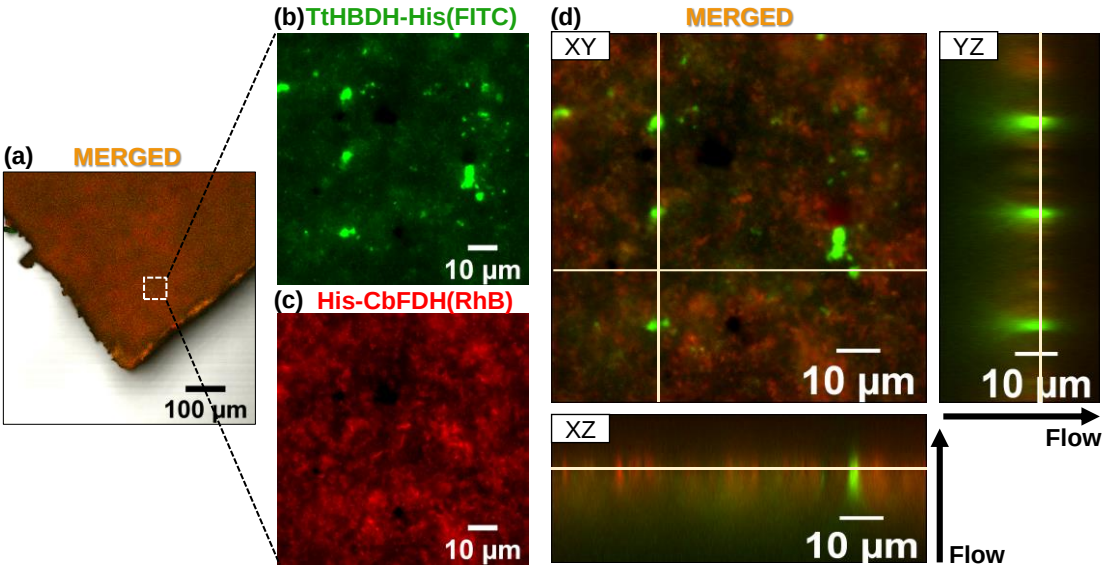

Figure 4: Confocal laser scanning microscopy images of the distribution of co-immobilized fluorophore-labeled enzymes on YSZ**.** (a) YSZ fragment overview where the region (white square) of imaging of panels (b) and (c) is depicted. (b) TtHBDH-His labeled with Fluorescein isothiocyanate (FITC, green channel) immobilized on YSZ. (c) His-CbFDH la with Rhodamine B (RhB, red channel) and co-immobilized on the same YSZ fragment. (d) *Ortho*-representation of CLSM z-stack images from YSZ with immobilized TtHBDH-His(FITC) and His- CbFDH(RhB) (merged channel).

the spatial correlation of signal intensity is very low and non-uniformly distributed across the YSZ surface (Figure S10). The lack of correlation between the signal of both enzymes points out that both enzymes follow different organization patterns across the YSZ surface. While TtHBDH-His(FITC) mainly localizes in small clusters with high density spotted through the surface, His-CbFDH(RhB) is less densely and more uniformly distributed across the surface. This different spatial distribution is supported by the low Pearson coefficient (0.281) (Table S3).

To further investigate the position of both enzymes across the 3D structure of the YSZ membrane, we performed a Z-stack of the sample through digitally reconstructing confocal planes at different heights of the sample (Figure 4d and Video S1). Figure 4d unveils that the first immobilized enzyme, TtHBDH-His(FITC) colonized the most

proximal regions to the inlet of the flow reactor and the pores with preferential fluid paths (larger pore size). On the contrary, the second enzyme (Rhodamine B labellabeled His-CbFDH) colonized the deeper and the inner regions of the YSZ membrane as the most accessible surface is already occupied by the first enzyme. The sequential immobilization of the two enzymes in flow explains this pattern, where the flow direction and the material design determine the final spatial organization of the heterogeneous biocatalyst. Although non investigated in this work, the immobilization kinetics also can control the enzyme spatial distribution across the surface as demonstrated for the batch immobilization of many proteins and enzymes.[40, 41] Likewise, our group previously showed that the immobilization kinetics can also be controlled by tunning the flow rate. In these studies, we demonstrated that flow rate is also another fundamental parameter to control the protein spatial distribution across the volume of a reactor bed formed by packed porous agarose microbeads.[42] Therefore, tunning the immobilization conditions in flow (flow rate and direction) emerges as an alternative to some lithographies for controlling the microscopic spatial distribution of immobilized multi-enzyme systems across flow reactors.[42, 43] Besides the immobilization sequence and flow rates, the spatial distribution of enzymes across porous carriers can also be tailored using tailoring of materials physicochemical

Continuous operational performance of dehydrogenases co-immobilized on naked YSZ

Before testing the orthogonal cooperation of His-CbFDH and TtHBDH-His co-immobilized on YSZ for bioredox cascades, we optimized the flow rate for each enzyme. YSZ membranes were loaded with 0.1 mg of each enzyme and operated at different flow rates 0.01 - 0.2 mL × min^{-1} to determine the operational limits and the optimal conditions for both enzymes. The range of residence time (τ) for the tested flow rates was 10-0.5 min. Figures 5a-b show the NADH and NAD^+ conversion catalyzed by the co-immobilized TtHBDH-His and His-CbFDH on naked YSZ membranes, respectively, as well as their corresponding recovered specific activity upon the immobilization process. We firstly assessed the reductive activity of the TtHBDH-His on the YSZ co-immobilized system by feeding the reaction with a reaction mix containing NADH and EAA. Immobilized TtHBDH-His exhibits high conversion rates (up to 90% of cofactor conversion) at a low flow rate and consequently longer residence time. Maximal immobilized specific activity was achieved at flow rates higher than 0.05 mL × min^{-1},

where immobilized TtHBDH-His recovered 70% of that specific activity measured for its free counterpart (Figure 5a). Therefore, the optimal balance between productivity and product conversion was found at 0.05 ml × min^{-1}. Likewise, we tested the oxidative performance of the co-immobilized His-CbFDH on YSZ by feeding the reactor with a reaction mix containing NAD^+ and formic acid. Unlike for TtHBDH-His, the conversion decay was less dramatic at increasing flow rate, and the recovered specific activity of co-immobilized His-CbFDH increased with the flow without reaching a plateau (Figure 5b).

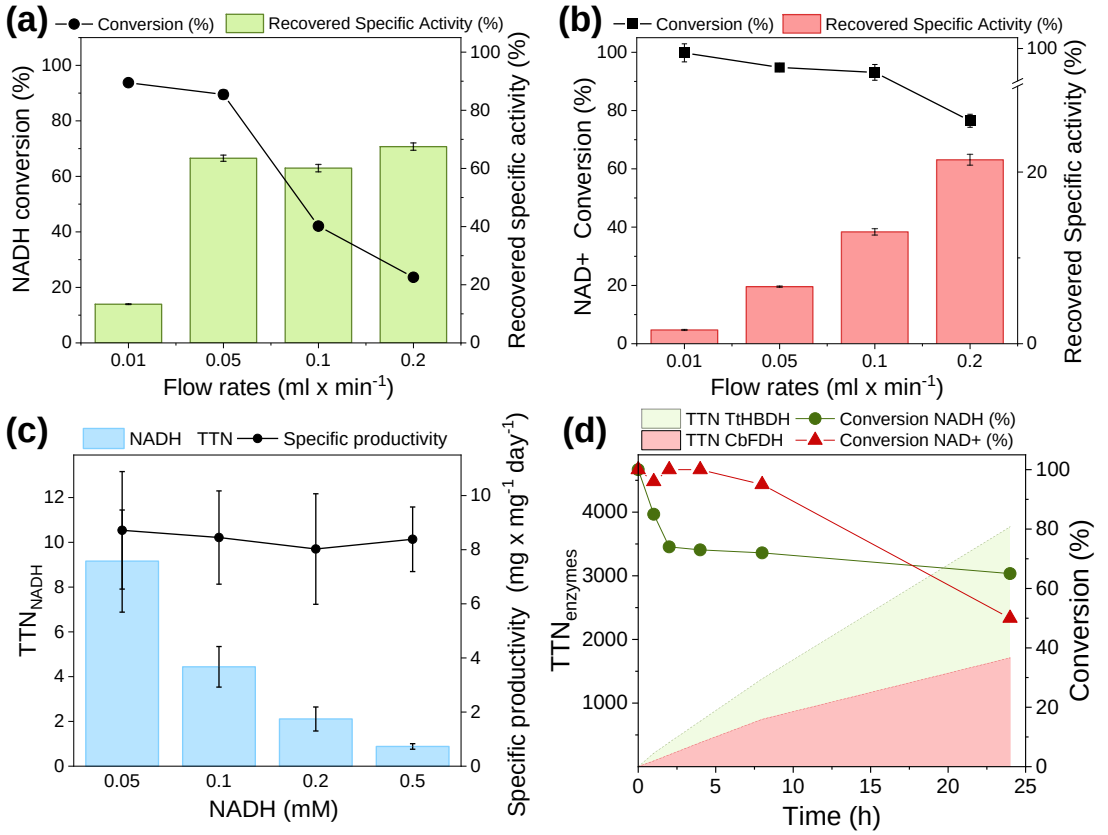

Figure 5: Continuous asymmetric reduction of EAA catalyzed by the TtHBDH-His and His-CbFDH co-immobilized on naked YSZ with *in situ* NADH recycling. (a) TtHBDH-His activity at different flow rates through measuring the conversion of NADH oxidation (%) and the relative recovered specific activity (%) regarding the soluble enzyme (0.14 U × mg^{-1}). (b) His-CbFDH activity at different flow rates through measuring the conversion of NAD^+ reduction (%) and the relative recovered specific activity (%) regarding the soluble enzyme (1 U × mg^{-1}) (c) Specific productivity of the bi-enzymatic system for the reduction of 10mM EAA to ethyl (*S*)-3-hydroxybutyrate with different NADH concentrations (0.05 - 0.5 mM) at 0.01 ml × min^{-1}. The accumulated NADH TTN value was calculated as the concentration of obtained (*S*)-3-hydroxybutyrate divided by the concentration of NADH. (d) Operational stability and TTN of TtHBDH-His and His-CbFDH immobilized on YSZ membrane tracked by NADH and NAD+ conversion during the reduction of 10mM EAA and the oxidation of 100mM formic acid respectively.

At the highest flow rate tested, His-CbFDH recovered only 20% of the specific activity measured for the soluble enzyme. These results indicate that even at 0.2 mL × min^{-1}, His-CbFDH is far from its maximal productivity. This low productivity suggests that an important population of immobilized His-CbFDH molecules are underutilized. Nevertheless, using 0.05 mL × min^{-1} as consensus flow rate, we guarantee an efficient redox cofactor recycling as His-CbFDH converts up to 90% of NAD^+ into NADH, assuring the maximal productivity of TtHBDH-His. When using lower flow rates, the longer residence times allow quantitatively converting 0.2 mM of nicotinamide cofactor in both reduction and oxidation directions, although both enzymes work far from their optimal conditions.

Next, we fed the reactor with a reaction mix containing 10 mM EAA, 100 mM sodium formate, and 0.2 mM NADH at 0.05 mL × min^{-1} to assess the orthogonality of this bi-functional heterogeneous biocatalyst in continuous operation. In this context, the co-immobilized His-CbFDH acts as the NADH recycling partner for TtHBDH-His to reduce EAA into ethyl (*S*)-3-hydroxybutyrate, oxidizing formic acid as an ancillary electron donor. Under those conditions, we achieved 0.37 mM of ethyl (*S*)-3-hydroxybutyrate, giving rise to a total NADH turnover number (TTN_{NADH} = mol of product/mol of NADH) of 1.84. When we decreased the flow rate to 0.01 mL × min^{-1}, the product yield raised to 0.43 mM and the TTN_{NADH} slightly increased to a value of 2. Although individual operational tests for co-immobilized TtHBDH-His and His-CbFDH suggested 0.05 mL × min^{-1} as flow rate, the orthogonal cascade reaction seems to demand 5 times slower flows as the cofactor must diffuse from one enzyme to the other within the porous microenvironment of the YSZ membrane. Such transport phenomena were missed when analyzing the activity of both enzymes individually. Thus, longer residence times (lower flow rate) enhance the final yield of the product when cofactor regeneration is needed.

Like in other immobilized bio-redox cascades,[41, 43, 44] the redox cofactor concentration affects both the specific cascade productivity and the TTN_{NADH}. To stress our redox enzyme cascade co-immobilized on YSZ membranes under limiting cofactor conditions, we analyzed the system performance in flow, using different cofactor concentrations. By determining the conversion of EAA into ethyl (*S*)-3-hydroxybutyrate at the reactor outlet using a flow rate of 0.01 mL × min^{-1}, we calculated the specific productivity and the TTN_{NADH} of the heterogeneous biocatalyst at different NADH

concentrations (Figure 5c). We found that the heterogeneous biocatalyst exhibits a specific productivity of roughly 8.4 $mg_{product} \times mg_{TtHBDH\text{-}His}^{-1} \times day^{-1}$ regardless of the NADH concentration. Furthermore, these data prove that the *in situ* cofactor regeneration works efficiently as the bulk cofactor concentration barely affects the overall system productivity. In fact, NADH molecules were recycled up to 9 times when cofactor concentration was as low as 0.05 mM. Similar TTN_{NADH} values have been previously reported for heterogeneous biocatalysts where the NADH was co-immobilized with different systems of dehydrogenases.[45, 46] To further demonstrate the versatility of YSZ membranes to site-selectively immobilized multi-enzyme systems, we co-immobilized an Alanine dehydrogenase from *Bacillus subtilis* (His-BsAlaDH) with His-CbFDH (Figure S11a). We analyzed the conversion of pyruvate into L-alanine using a flow rate of 0.01 $mL \times min^{-1}$ by HPLC (Figure S11b). As result, the YSZ reactor exhibited a specific productivity of 64 $mg_{product} \times mg_{His\text{-}BsAlaDH}^{-1} \times day^{-1}$ recycling each NADH molecule up to 5 times.

Finally, we tested the operational stability of TtHBDH-His as a standalone enzyme immobilized on the YSZ membrane. To that aim, we performed the asymmetric reduction of EAA without cofactor recycling. Figure 5d shows that after a sharp initial drop in NADH conversion, more than 60% of TtHBDH-His initial activity is retained after 24h of continuous operation at room temperature. As a result, the accumulated TTN of the immobilized Tt27-HBDH almost reached a value of 4000 in 24h of continuous use. This value is similar to that one obtained for consecutive recycling of the untagged TtHBDH on agarose beads activated with aldehyde groups and coated with polyethyleneimine.[25] This suggests that immobilization on YSZ supports is not detrimental to the intrinsic stability of the thermostable TtHBDH-His. Unfortunately, such good operational stability cannot be matched by the His-CbFDH immobilized on naked YSZ (Figure 5d, 50% activity lost after 24 h with a maximum $TTN_{Cb\text{-}FDH}$ of 1500)), suggesting that the mesophilic origin of the recycling dehydrogenase is the Achilles' heel of the herein presented systems. Further efforts to search for more thermostable Formate dehydrogenase must be done to match the operational stability of both dehydrogenases within the YSZ porous surface.

CONCLUSION

Co-immobilization of reaction cascades is an attractive solution for modern chemical manufacturing. Hence new cost-efficient and robust materials are in demand to achieve site-selective immobilization of several enzymes within the same porous surface. In this work, we have fabricated a YSZ scaffold with a thin disk shape to co-immobilize a bioredox cascade formed by two dehydrogenases. Although our first intention was infiltrating the YSZ material with nickel oxide nanoparticles to drive the immobilization through a His-tag fused to either terminus of the enzymes, we discovered that His-tagged enzymes were not only immobilized but also did it more efficiently on naked YSZ surfaces than on NiO infiltrated YSZ. After deeper investigations based on competitive assays and XPS, we found that the imidazole rings of the His-tag selectively interact with the Zr and Y atoms at the surface of YSZ scaffolds. The mechanism of this interaction needs further investigation to better understand the nature of the coordination bonds. Nevertheless, these results prove for the first time that YSZ porous scaffolds can directly immobilize His-tagged enzymes in flow, without previous functionalization, and in a very selective manner. We then expanded the utility of these YSZ materials to the co-immobilization of two His-tagged dehydrogenases in flow to assemble a parallel bioredox cascade with *in situ* cofactor recycling. Besides characterizing the specific productivity of each immobilized enzyme, confocal fluorescence microscopy analysis revealed a non-uniform distribution and poor microscopic co-localization of both enzymes through the 3D porous surface of the YSZ membrane. In view of these studies, we conclude that the immobilization sequence and the direction of the flow are fundamental parameters to control the spatial patterns of the co-immobilized enzymes. Finally, we optimized the flow rate and the NADH concentration to maximize the specific productivity of the bi-enzymatic cascade as well as the total turnover number of the cofactor. This new YSZ-material has demonstrated an extraordinary versatility to efficiently immobilize His-tagged enzyme cascades for their application in the continuous manufacturing of high-added value chemicals. Although the productivity achieved with one single membrane disk is still too low for practical purposes, the versatility of this system to be telescoped forecasts its scalability without losing control of the convective-diffusive flow. Moreover, an advanced design of the internal morphology can give us further control over the flow dynamics of the system to improve the spatial enzyme distribution and thus the performance of the immobilized enzyme. Hence, we foresee that the simplicity and the selectivity of this immobilization protocol will encourage other scientists to use this

inorganic material as a carrier for assembling heterogeneous biocatalysts in flow-reactors for continuous processes.

MATERIALS AND METHODS

Materials

8 mol.% Y_2O_3 stabilized zirconia (TZ-8YS®) was acquired from TOSOH (Japan) and nickel oxide (NiO) from Alfa Aesar GmbH (Kandel, Germany). Ammonium salt of poly(methacrylic acid) (PMMA) was supplied as 25 wt.% active matter concentration solution in water (Darvan® C-N) by Vanderbilt Minerals LLC (Gouverneur, NY, USA). Acrylic polymer-based binders (Duramax® B-1000 with Tg = −26 and Duramax® B-1022 with Tg = 39) were acquired from Rohm and Haas Company (Philadelphia, Pennsylvania, USA). Graphite powder (UF-2) with particle size of d_{V50}=4–5 µm, was purchased from Graphit Kropfmühl GmbH (Hauzenberg, Germany). Marfey´s reagent (Thermo Scientific, Whatlman, MA, USA)

Ethyl acetoacetate (EAA), pyruvate, nickel (II) nitrate hexahydrate, sodium formate, and other reagents were supplied by Sigma-Aldrich (St. Louis, IL, USA). Nicotinamide adenine dinucleotides (NAD^+, NADH) were purchased from GERBU Biotechnik GmbH (Heidelberg, Ger). Protein concentrations were determined using Bradford Assay from Bio-Rad Laboratories Inc. (Hercules, CA, USA). Absorbance measures were carried out with an Epoch 2 Microplate Spectrophotometer from Biotek® Instruments Inc. (Winooski, VT, USA). Inject® Syringes were purchased from Braun (Melsungen, Ger). Genes encoding an N-term His-tagged formate dehydrogenase (His-CbFDH) from *Candida boidinii* and L-Alanine dehydrogenase from *Bacillus stearothermophilus,*[28] and a C-terminus His-tagged 3-hydroxybutyryl-CoA dehydrogenase from Thermus thermophilus HB27[27] (TtHBDH-His) were *E.coli* codon optimized and synthesizedinus by GenScript (Piscataway, USA) and cloned into pET28b plasmid. The protein sequences of these proteins are provided in Figure S12.

Preparation of YSZ based membranes

Planar geometry highly porous yttrium stabilized zirconia (YSZ) materials as a starting scaffold for YSZ based membranes were prepared through tape casting technique. For this purpose, water based colloidal suspension with commercial YSZ, NiO, and graphite powders were prepared. As received YSZ and NiO powders were mixed in the

proportion of solid matter (70 vol.% YSZ– 30 vol.% NiO) and dispersed in distilled water at an initial solid loading of 50 vol.% with 1.8 wt.% Darvan® C-N as surfactant. The obtained suspension was ball milled for 24 h with zirconia ball milling media. The two binders (Duramax® B-1000 and B-1022) were added (7 wt.% of solids, each) and the suspension was homogenized with centrifugal mixer (Thinky ARE-250, Japan). Finally, the graphite powder UF-2 was added (20 vol.% of solids) and the suspension was further homogenized with cena trifugalhe mixer. Tape casting of obtained suspension was performed on Mylar sheets with a blade gap of 600 µm. Tapes were left to dry for 24 h before shaping to circular shapes (diameter 14 mm) and sintered in air at 1300 ºC with the dwelling time of 4 h, resulting in final membrane geometries with a diameter of ~10 mm and thickness of ~300 µm. To achieve highly porous YSZ scaffold, both, graphite and NiO phases, were deployed as sacrificial pore formers. Graphite is added to generate initial porosity within sintered YSZ-NiO composite, whereas the NiO phase is eliminated from sintered composite through a procedure first reported by Kim. H et al.[47] For this, YSZ-NiO composite is subjected to temperature induced reduction with 2% H_2/Argon gas at 800 °C (dwell 4 h) and obtained YSZ-Ni cermet is leached twice with 33% nitric acid, removing Ni phase, resulting in YSZ porous structure. Infiltration of nanometric range nickel oxide nanoparticles to YSZ based membranes was done by vacuum infiltration once (np x1), twice (np x2) or four (np x4) times with 3M solution of Nickel (II) nitrate hexahydrate with intermediate thermal treatment steps at 400 º C (dwell 1 h) to decompose nitrate precursor. Nickel nanoparticle infiltrated YSZ membranes were subjected to the final thermal treatment step at 600 ºC (dwell 2h) to eliminate residual carbonaceous species and to consolidate the formed nickel oxide nanoparticle phase within the YSZ backbone.

Microstructural characterization of YSZ based membranes

Microstructural characterization of obtained membranes was done on representative polished cross section samples through Scanning Electron Microscopy (SEM) analysis with Jeol JSM 6010 Microscope (JEOL, Ltd, Tokyo, Japan).

YSZ based membrane reactor set-up

Circular YSZ based membranes with a 20 mm radius and ~0.3 mm in width were mounted to an in-line polycarbonate filter holder with a liquid latex seal at the borders.

The effective volume of the mounted membranes (membrane reactor) was ≈ 0.1 cm^3. Reaction mixtures or enzyme solutions were pumped to the reactor with a syringe pump 11-PLUS, Harvard apparatus (MA, USA). Enzymes and substrates were flushed through the membrane reactors and samples were collected in the outlet at different time points according to the experimental design.

TtHBDH and TtHBDH-His production and purification

Wild-type TtHBDH and its His-tagged variant (TtHBDH-His) were expressed and purified as described elsewhere.[27] Briefly, pET28b plasmids encoding the corresponding enzymes (Figure S12) were transformed in BL21 (DE3) *E. coli* cells. Colonies were picked and grown in LB containing kanamycin (30 μg × mL^{-1}). When an optical density (OD_{600}) of 0.6 was reached, 1 mM IPTG (isopropyl-β-D-thiogalactopyranoside) was added to induce the protein expression. The induced cultures were grown for 3 h at 37 °C and the bacteria were harvested by centrifugation. Then, the cells were resuspended in 25 mM phosphate buffer pH 7 and lysed by sonication. The cell debris was discarded by centrifugation (10 000 × g for 20 min) and the soluble crude protein extract was incubated at 70 °C for 45 min to purify the thermophilic enzyme through thermal shock as previously described.[27] The pellets of denatured mesophilic proteins were discarded after centrifugation (10 000 × g for 30 min).

His-CbFDH and His-BsAlaDH production and purification

His-CbFDH and His-BsAlaDH (Figure S12) were overexpressed in E. coli BL21 (DE3) as described elsewhere.[28] Briefly, cells transformed with the corresponding plasmids were grown at 21 °C until an OD_{600} of 0.6 was reached. Then, the enzyme expression was induced with 1 mM IPTG, and the culture was incubated at 21 °C for 18 h. The cells were harvested by centrifugation and lysed by sonication. The pellet was discarded and the supernatant containing the soluble crude protein extract was purified through IMAC chromatography using agarose microbeads functionalized with iminodiacetic cobalt chelates (ABT, Madrid, Spain). Protein was eluted with 25 mM phosphate and 300 mM imidazole buffer pH 7 at 4 ºC. Imidazole was removed from purified enzymes by gel-filtration using a PD-10 column (GE healthcare, Chicago, IL, USA), the protein was eluted with 25mM sodium phosphate buffer pH 7.

Determination of the concentration of soluble enzymes

The determination of the concentration of soluble enzyme (TtHBDH, TtHBDH-His, His-CbFDH, or His-BsAlaDH) was carried out with Bradford protein assay (Bio-Rad, Ca, USA) reagent. A commercial solution of bovine serum albumin (Sigma-Aldrich, St. Louis, IL, USA) was used to determine a standard curve. 5 µL of soluble enzyme solution was mixed with 200 µL of Bradford reagent. After 5 minutes of incubation, the absorbance was measured at 595 nm at room temperature.

Spectrophotometric activity assays of soluble enzymes

The enzymatic activities of soluble enzymes were spectrophotometrically measured in 96-well plates by monitoring the absorbance at 340 nm.

TtHBDH activity assay. 5 µL of enzyme solution (0.1 mg × mL^{-1}) were incubated with 200 µL of a solution of 10 mM of EAA and 0.2 mM NADH in 25 mM phosphate buffer pH 7 at 30 ºC. One TtHBDH-His unit (U) was defined as the amount of enzyme required to reduce 1 µmol of NADH per minute under given conditions and considering an ε = 6.22 $mM^{-1} \times cm^{-1}$ for NADH at 340 nm.

CbFDH activity assay. 5 µL of enzyme solution (0.1 mg × mL^{-1}) were incubated with 200 µL of a solution of 1 mM of NAD^+ and 100 mM Sodium formate in 25 mM phosphate buffer pH 7, at 30 ºC. One His-CbFDH unit (U) was defined as the amount of enzyme required to oxidize 1 µmol of NAD^+ per minute under given conditions and considering an ε = 6.22 $mM^{-1} \times cm^{-1}$ for NADH at 340 nm.

In flow enzyme immobilization on YSZ based membrane reactors

First, YSZ based membrane reactors were equilibrated with 10 mL of 25 mM sodium phosphate buffer at pH 7. Depending on the experiment (activity or load tests), 1-2 mL of 0.1-0.5 mg × mL^{-1} enzyme solution were flushed through a membrane reactor at 0.02 mL × min^{-1} and room temperature. 0.1 mL aliquots were collected, and the presence of protein was determined by the Bradford protein assay. After immobilization, the membrane reactors were washed with 10 mL of 25 mM sodium phosphate buffer at pH 7 at the same flow rate. For co-immobilization experiments, YSZ based membrane reactors already harboring TtHBDH-His were equilibrated with 10 mL of 25 mM sodium phosphate buffer at pH 7, and then flushed with 0.1-0.5 mg of His-CbFDH in 25 mM phosphate buffer at pH 7 solution at 0.02 mL × min^{-1} and room temperature. Like for the His-TtHBDH, 0.1 mL aliquots were collected, and the presence of protein and activity

were determined by Bradford Protein and colorimetric activity assay, respectively. After immobilization, the YSZ based membrane reactors were washed with 10 mL of 25 mM sodium phosphate buffer at pH 7 and stored at 4 ºC. The same protocol was followed to sequentially co-immobilize the bi-enzyme system His-AlaDH and His-CbFDH.

Desorption of immobilized enzymes from YSZ based membrane reactors.

YSZ based membrane reactors with immobilized enzymes were equilibrated with 10 mL of 25 mM sodium phosphate buffer at pH 7 at room temperature. Then 2 mL of different solutions: 25 mM sodium phosphate buffer pH 7, 1M NaCl, or 1M Imidazole was passed through the YSZ based membrane reactors at 0.02 mL × min^{-1} and room temperature. 0.1 mL aliquots were collected, and their protein concentration was analyzed by Bradford assay. The aliquots in which protein presence was measured were analyzed by SDS-PAGE.

X-ray photoelectron spectroscopy (XPS)

XPS experiments were performed in a SPECS Sage HR 100 spectrometer with a non-monochromatic X-ray source (Aluminium Kα line of 1486.6 eV energy and 300 W), placed perpendicular to the analyzer axis and calibrated using the 3d5/2 line of Ag with a full width at half maximum (FWHM) of 1.1 eV. The selected resolution for the spectra was 15 eV of Pass Energy and 0.15 eV/step. All measurements were made in an ultra-high vacuum (UHV) chamber at a pressure of around $8 \cdot 10^{-8}$ mbar. CasaXPS was used for deconvoluting data. C 1s peak from C-C sp3 of adventitious carbon was employed for charge correction fixing its BE to 284.8 eV. A Shirley background was applied.

Enzyme fluorescent labeling

Fluorescent labeling of His-tagged TtHBDH and His-CbFDH with FITC (Fluorescein isothiocyanate) and RhB (Rhodamine B Isothiocyanate), respectively was done based on protocols described elsewhere.[48] Briefly, enzyme solution in 100 mM sodium bicarbonate buffered solution at pH 8.5 was mixed with RhB/FITC solution in DMSO (1:10 molar ratio) and incubated for 1 h under gentle shaking at 25 ºC. The remaining fluorophore was eliminated by filtering the enzyme solution in a tangential

ultrafiltration unit (10 KDa) with 25 mM sodium phosphate buffered solution at pH 7 until no fluorescence was detected in the filtered solution. Immobilization of the labeled enzyme was done in flow as previously described for the non-labeled enzymes.

Confocal laser scanning microscopy (CLSM)

Spatial organization of FITC-labelled TtHBDH-His co-immobilized with RhB-labelled His-CbFDH was followed using a confocal laser scanning microscopy with a ZEISS LSM 880 (Carl Zeiss, Germany) and excitation lasers of λ_{ex} = 488 nm for FITC and λ_{ex} = 561 nm for RhB.

Image processing and analysis

Image processing and analysis were done using FIJI (Image J) software.[49] Co-localization and correlation analysis of immobilized labeled enzymes was done using the following FIJI plugins: Colocalization Colormap[50] and JACoP.[48] The co-localization colormap allows the quantification of correlation while maintaining the spatial information about the co-localization of the fluoresce intensity signal of the two channels (channel 1: FITC and channel 2: RhB). The plugin calculates the normalized mean deviation product (nMDP) for each pixel. This parameter provides a correlation between the intensity of both channels based on the algorithm described by Jaskolski et al.[51] The plugin provides a graphic representation of the nMDP index whose values range from −1 to 1. Positive values of the index represent correlated pixels, meanwhile, negative values indicate the absence of correlation. JACoP plugin was used to calculate Manders' and Pearson's coefficients. Manders' indicates the proportion of one signal coincidence with the signal of the second channel over its total intensity. Pearson's coefficient indicates the relationship between the intensities of two images, providing a rate of association of two fluorochromes which ranges from -1 to 1, indicating negative (-1), positive (+1), or null (0) correlation.

Determination of enzyme activity in the flow

To analyze the activity of immobilized TtHBDH-His, a reaction mix (10 mM of EAA and 0.2 mM NADH in 25 mM phosphate buffer pH 7) was flushed through the YSZ

based membrane reactor at different flow rates (0.01, 0.05, 0.1, 0.2 mL × min^{-1}) at room temperature. The residence times (t) for these flow rates were 10, 5, 1, and 0.5 min, respectively. 0.1 mL aliquots were collected and the consumed NADH concentration was measured spectrophotometrically at 340 nm (ε = 6.22 $mM^{-1} \times cm^{-1}$). One TtHBDH-His unit (U) was defined as the amount of enzyme required to consume 1 μmol of NADH per minute under reaction conditions. Likewise, the activity of immobilized His-CbFDH was measured flushing a reaction mix (100 mM of sodium formate, 0.2 mM NAD+ in 25 mM phosphate buffer pH 7) through the YSZ based reactors at different flow rates (0.01, 0.05, 0.1, 0.2 mL min^{-1}), giving rise to the same residence time as described above. Like for TtHBDH-His, 0.1 mL aliquots and the produced NADH concentration was measured spectrophotometrically at 340 nm (ε = 6.22 $mM^{-1} \times cm^{-1}$). One His-CbFDH unit (U) was defined as the amount of enzyme required to produce 1 μmol of NADH per minute under reaction conditions.

Asymmetric reduction of EAA in flow integrating NADH recycling systems.

A reaction mix (10 mM EAA, 100 mM sodium formate, and 0.01-0.5 mM NADH in 25 mM phosphate buffer pH 7) was flushed through the YSZ based membrane reactors at 0.01 mL × min^{-1}. 0.3 mL aliquots were collected and analyzed by gas chromatography with flame ionization detector (GC-FID) Briefly, every sample was subjected to liquid-liquid extraction with dichloromethane in a ratio of 1:1 *(v:v)* and the aqueous phase was discarded. 30–50 mg of anhydrous $MgSO_4$ were added to the organic phase to dry the samples. 2 mM Eicosane was added as an internal standard before the GC-FID analysis. Analyses were carried out in an Agilent 8890 gas chromatography system using a column of (5%-phenyl)-methylpolysiloxane (Agilent, J&W HP-5 30 m × 0.32 mm × 25 μm), helium as carrier gas (1.5 ml × min^{-1}), and equipped with an FID detector. The temperatures of the injector and FID detector were 280 °C and 300 °C, respectively. The separation of compounds was carried out by two sequential temperature ramps: the initial temperature (60 °C) was maintained for 2 min and progressively increased up to 160 °C at a rate of 10 °C × min^{-1}. Then, the column temperature was increased 20 °C × min^{-1} for 4 min until 250 °C and maintained for 4 min. Retention times were 5.2 min for ethyl acetoacetate and 5.08 min for ethyl 3-(*S*)-hydroxybutyrate.

We assessed the specific productivity of the biocatalyst defined as the mg of product generated by 1 mg of TtHBDH-His immobilized on YSZ membrane per day ($mg_{product} \times mg_{TtHBDH\text{-}His}^{-1} \times$ **day**$^{-1}$) and the total turnover number of NADH (TTN_{NADH}) defined as

mol of 3-(*S*)-hydroxybutyrate obtained per mol of NADH supplied with the reaction media.

Asymmetric reduction of Pyruvate in flow integrating NADH recycling systems.

A reaction mix (100 mM Pyruvate, 400 mM Ammonium Formate, and 1 mM NADH in 200 mM phosphate buffer pH 7) was flushed through the YSZ based membrane reactors at 0.01 mL × min^{-1} (Figure S11). 0.3 mL aliquots were collected and analyzed by HPLC. The synthesized alanine was derivatized with the Marfey reagent. Briefly, properly diluted reaction sample (20 µL) was mixed with sodium bicarbonate (8 µL, 1 M) and the Marfey´s reagent diluted in acetone (20 µL, 15 mM) and incubated for 1 h at 50 °C and 400 rpm. Afterward, the derivatization reaction was stopped by the addition of HCl (8 µL, 2 M), then centrifuged at 13450 g for 10 min, and the supernatant was properly filtered to perform the HPLC analysis. Derivatized samples were analyzed in an HPLC Agilent Technologies 1260 Infinity, with a Poroshell EC-C18 column (4.6 ×100 mm, 2.7µm) at a flow rate of 1 mL x min^{-1}. Mobile phases: A: Acetonitrile, and B: trifluoroacetic acid 0.1 % in water. Elution was conducted as follows: starting from 10 % A and 90 % B to reach a composition of 20 % A in 17 min. That mobile phase composition was maintained for 3 min; then A% was increased from 20% until 40 % in 20 minutes, and finally, the initial conditions (10% A) were recovered in 20 min. Detection of compounds was performed at λ=340 nm. The retention time for derivatized L-alanine was 25.6 min. The degree of conversion was calculated by fitting the area of the peak with a calibration curve under the same elution conditions.

We assessed the specific productivity of the biocatalyst defined as the mg of product generated by 1 mg of His-BsAlaDH immobilized on YSZ membrane per day ($mg_{product}$ × $mg_{BsAlaDH}^{-1}$ × $\mathbf{day}^{-1}$) and the total turnover number of NADH (TTN_{NADH}) defined as mol of L-Alanine obtained per mol of NADH supplied with the reaction media.

Determination of operational stability of dehydrogenases immobilized on naked YSZ

We determined the operational stability and the total turnover number of TtHBDH-His or His-CbFDH ($TTN_{enzymes}$). The TTNs were defined as the mol of NADH or NAD+ consumed per mol of TtHBDH-His or His-CbFDH respectively. The naked

YSZ reactors with the immobilized enzymes were operated for 24 hours at a fixed flow rate of 0.01 mL × min -1 flushing 10 mM EAA and 1 mM NADH and 100 mM formic acid and 1mM NAD+ for TtHBDH-His and His-CbFDH, respectively, to determine their activity determination in flow. The conversions were determined spectrophotometrically as described above.

Supporting Information.

The supporting information includes the enzyme primary sequences, SDS-PAGE analysis of enzyme YSZ interactions, XPS additional data, and confocal fluorescence microscopy analysis

AUTHOR INFORMATION

Corresponding Authors

Fernando López-Gallego: flopez@cicbiomagune.es

Jonas Gurauskis: jonas.gurauskis@csic.es

AUTHOR CONTRIBUTIONS

Experiments were performed by DAS, ED, DS and JG. The manuscript was written by DAS and FLG. The work was conceptualized by JG and FLG. Funding was secured by FLG. All authors discussed the results and revised the manuscript. All authors have approved the final version of the present manuscript.

Notes

The authors declare no competing financial interest.

ACKNOWLEDGMENTS

ERC-Co (METACELL-818089)) project is acknowledged for funding. FLG thanks IKERBASQUE for sponsoring him. This work was performed under the Maria de Maeztu Units of Excellence Program from the Spanish State Research Agency—grant no. MDM-2017-0720 (CIC biomaGUNE). We thank Dr. Susana Velasco Lozano for her assistance with the HPLC analysis.

ABBREVIATIONS

Yttrium-stabilized zirconia (YSZ); Nickel oxide (NiO); 3-Hydroxybutyryl-CoA dehydrogenase from *Thermus termophilus* (TtHBDH); TtHBDH with a fused 6x Polyhistidine tag in C-terminal (TtHBDH-His); Formate dehydrogenase from *Candida boidinii* with a fused 6x Polyhistidine tag in N-terminal (His-CbFDH); Total turnover number (TTN); Packed-bed reactors (PBRs); 3-aminopropyltriethoxysilane (APTES); NiO nanoparticles (NiOnp); Scanning electron microscopy (SEM); YSZ membranes with 1, 2 or 4 NiOnp infiltration cycle (YSZ-NiOnp x1; x2; x4); Polyacrylamide-agarose gel electrophoresis with SDS. (SDS-PAGE); X-ray photoelectron spectroscopy (XPS); Ethyl acetoacetate (EAA); Confocal laser scanning microscopy (CLSM); Fluorescein isothiocyanate (FITC); Rhodamine B (RhB); Energy Dispersive X-Ray (EDX); Nicotinamide adenine dinucleotides (NAD+, NADH); Enzymatic unit of activity (U); Alanine dehydrogenase from *Bacillus subtilis* (His-AlaDH)

REFERENCES

1. Britton, J.; Majumdar, S.; Weiss, G. A., Continuous Flow Biocatalysis. *Chem. Soc. Rev.* **2018,** *47*, 5891-5918.
2. De Santis, P.; Meyer, L.-E.; Kara, S., The Rise of Continuous Flow Biocatalysis – Fundamentals, Very Recent Developments and Future Perspectives. *React. Chem. Eng.* **2020,** *5*, 2155-2184.
3. Tamborini, L.; Fernandes, P.; Paradisi, F.; Molinari, F., Flow Bioreactors as Complementary Tools for Biocatalytic Process Intensification. *Trends Biotechnol.* **2018,** *36*, 73-88.
4. Thompson, M. P.; Peñafiel, I.; Cosgrove, S. C.; Turner, N. J., Biocatalysis Using Immobilized Enzymes in Continuous Flow for the Synthesis of Fine Chemicals. *Org. Process Res. Dev.* **2019,** *23*, 9-18.
5. Benítez-Mateos, A. I.; Contente, M. L.; Roura Padrosa, D.; Paradisi, F., Flow Biocatalysis 101: Design, Development and Applications. *React. Chem. Eng.* **2021,** *6*, 599-611.
6. Bolivar, J. M.; López-Gallego, F., Characterization and Evaluation of Immobilized Enzymes for Applications in Flow Reactors. *Curr. Op. Green. Sustain. Chem.* **2020,** *25*, 100349.
7. Ma, S.; Li, Y.; Ma, C.; Wang, Y.; Ou, J.; Ye, M., Challenges and Advances in the Fabrication of Monolithic Bioseparation Materials and Their Applications in Proteomics Research. *Adv. Mater.* **2019,** *31*, 1902023.
8. Hahn, R.; Panzer, M.; Hansen, E.; Mollerup, J.; Jungbauer, A., Mass Transfer Properties of Monoliths. *Sep. Sci. Technol.* **2002,** *37*, 1545-1565.
9. Kayvani Fard, A.; McKay, G.; Buekenhoudt, A.; Al Sulaiti, H.; Motmans, F.; Khraisheh, M.; Atieh, M., Inorganic Membranes: Preparation and Application for Water Treatment and Desalination. *Materials* **2018,** *11*, 74.

10. Zdarta, J.; Meyer, A. S.; Jesionowski, T.; Pinelo, M., A General Overview of Support Materials for Enzyme Immobilization: Characteristics, Properties, Practical Utility. *Catalysts* **2018,** *8*, 92.
11. Sigurdardóttir, S. B.; Lehmann, J.; Ovtar, S.; Grivel, J.-C.; Negra, M. D.; Kaiser, A.; Pinelo, M., Enzyme Immobilization on Inorganic Surfaces for Membrane Reactor Applications: Mass Transfer Challenges, Enzyme Leakage and Reuse of Materials. *Adv. Synth. Catal.* **2018,** *360*, 2578-2607.
12. Van den Biggelaar, L.; Soumillion, P.; Debecker, D. P., Enantioselective Transamination in Continuous Flow Mode with Transaminase Immobilized in a Macrocellular Silica Monolith. *Catalysts* **2017,** *7*, 54.
13. Chevalier, J.; Gremillard, L.; Virkar, A. V.; Clarke, D. R., The Tetragonal-Monoclinic Transformation in Zirconia: Lessons Learned and Future Trends. *J. Am. Ceram. Soc.* **2009,** *92*, 1901-1920.
14. Hannink, R. H. J.; Kelly, P. M.; Muddle, B. C., Transformation Toughening in Zirconia-Containing Ceramics. *J. Am. Ceram. Soc.* **2000,** *83*, 461-487.
15. Zeuner, B.; Ovtar, S.; Persson, Å. H.; Foghmoes, S.; Berendt, K.; Ma, N.; Kaiser, A.; Negra, M. D.; Pinelo, M., Surface Treatments and Functionalization of Metal-Ceramic Membranes for Improved Enzyme Immobilization Performance. *J. Chem. Technol. Biotechnol.* **2020,** *95*, 993-1007.
16. Grazú, V.; López-Gallego, F.; Montes, T.; Abian, O.; González, R.; Hermoso, J. A.; García, J. L.; Mateo, C.; Guisán, J. M., Promotion of Multipoint Covalent Immobilization through Different Regions of Genetically Modified Penicillin G Acylase from E. Coli. *Process Biochem.* **2010,** *45*, 390-398.
17. Abian, O.; Grazú, V.; Hermoso, J.; González, R.; García, J. L.; Fernández-Lafuente, R.; Guisán, J. M., Stabilization of Penicillin G Acylase from *Escherichia Coli*: Site-Directed Mutagenesis of the Protein Surface to Increase Multipoint Covalent Attachment. *Appl. Environ. Microbiol.* **2004,** *70*, 1249-1251.
18. Montes, T.; Grazú, V.; Manso, I.; Galán, B.; López-Gallego, F.; González, R.; Hermoso, J. A.; García, J. L.; Guisán, J. M.; Fernández-Lafuente, R., Improved Stabilization of Genetically Modified Penicillin G Acylase in the Presence of Organic Cosolvents by Co- Immobilization of the Enzyme with Polyethyleneimine. *Adv. Synth. Catal.* **2007,** *349*, 459-464.
19. Lin, Y.-C.; Liang, M.-R.; Lin, Y.-C.; Chen, C.-T., Specifically and Reversibly Immobilizing Proteins/Enzymes to Nitriolotriacetic-Acid-Modified Mesoporous Silicas through Histidine Tags for Purification or Catalysis. *Chem. Eur. J.* **2011,** *17*, 13059-13067.
20. Acquah, C.; Obeng, E. M.; Agyei, D.; Ongkudon, C. M.; Moy, C. K. S.; Danquah, M. K., Nano-Doped Monolithic Materials for Molecular Separation. *Separations* **2017,** *4*, 2.
21. Wu, Z.; Qi, W.; Wang, M.; Wang, Y.; Su, R.; He, Z., Chelate Immobilization of Amylase on Metal Ceramic Powder: Preparation, Characterization and Application. *Biochem. Eng. J.* **2013,** *77*, 190-197.
22. Wu, Z.; Qi, W.; Wang, M.; Su, R.; He, Z., Lipase Immobilized on Novel Ceramic Supporter with Ni Activation for Efficient Cinnamyl Acetate Synthesis. *J. Mol. Catal. B: Enzym.* **2014,** *110*, 32-38.
23. Serve, A.; Boreave, A.; Cartoixa, B.; Pajot, K.; Vernoux, P., Synergy between Ag Nanoparticles and Yttria-Stabilized Zirconia for Soot Oxidation. *Appl. Catal., B* **2019,** *242*, 140-149.
24. Ling, D.; Gao, L.; Wang, J.; Shokouhimehr, M.; Liu, J.; Yu, Y.; Hackett, M. J.; So, P.-K.; Zheng, B.; Yao, Z.; Xia, J.; Hyeon, T., A General Strategy for Site-

Directed Enzyme Immobilization by Using Nio Nanoparticle Decorated Mesoporous Silica. *Chem. Eur. J.* **2014,** *20*, 7916-7921.
25. Bodelón, G.; Mourdikoudis, S.; Yate, L.; Pastoriza-Santos, I.; Pérez-Juste, J.; Liz-Marzán, L. M., Nickel Nanoparticle-Doped Paper as a Bioactive Scaffold for Targeted and Robust Immobilization of Functional Proteins. *ACS Nano* **2014,** *8*, 6221-6231.
26. Li, Z.; Zhang, Y.; Su, Y.; Ouyang, P.; Ge, J.; Liu, Z., Spatial Co-Localization of Multi-Enzymes by Inorganic Nanocrystal–Protein Complexes. *Chem. Commun.* **2014,** *50*, 12465-12468.
27. Orrego, A. H.; Andrés-Sanz, D.; Velasco-Lozano, S.; Sanchez-Costa, M.; Berenguer, J.; Guisan, J. M.; Rocha-Martin, J.; López-Gallego, F., Self-Sufficient Asymmetric Reduction of B-Ketoesters Catalysed by a Novel and Robust Thermophilic Alcohol Dehydrogenase Co-Immobilised with Nadh. *Catal. Sci. Tech.* **2021,** *11*, 3217-3230.
28. da Silva, E. S.; Gómez-Vallejo, V.; Baz, Z.; Llop, J.; López-Gallego, F., Efficient Enzymatic Preparation of 13n-Labelled Amino Acids: Towards Multipurpose Synthetic Systems. *Chem. Eur. J.* **2016,** *22*, 13619-13626.
29. Gil, V.; Gurauskis, J.; Deleebeeck, L.; Stamate, E.; Hansen, K. K., Cathode-Supported Hybrid Direct Carbon Fuel Cells. *Int. J. Hydrogen Energy* **2017,** *42*, 4311-4319.
30. Hajimohammadjafartehrani, M.; Hosseinali, S. H.; Dehkohneh, A.; Ghoraeian, P.; Ale-Ebrahim, M.; Akhtari, K.; Shahpasand, K.; Saboury, A. A.; Attar, F.; Falahati, M., The Effects of Nickel Oxide Nanoparticles on Tau Protein and Neuron-Like Cells: Biothermodynamics and Molecular Studies. *Int. J. Biol. Macromol.* **2019,** *127*, 330-339.
31. Hoog Antink, M. M.; Beutel, S.; Rezwan, K.; Maas, M., Tailoring Electrostatic Surface Potential and Adsorption Capacity of Porous Ceramics by Silica-Assisted Sintering. *Materialia* **2020,** *12*, 100735.
32. Engelmark Cassimjee, K.; Kadow, M.; Wikmark, Y.; Svedendahl Humble, M.; Rothstein, M. L.; Rothstein, D. M.; Bäckvall, J. E., A General Protein Purification and Immobilization Method on Controlled Porosity Glass: Biocatalytic Applications. *Chem. Commun.* **2014,** *50*, 9134-9137.
33. Sanchez-Cano, C.; Alvarez-Puebla, R. A.; Abendroth, J. M.; Beck, T.; Blick, R.; Cao, Y.; Caruso, F.; Chakraborty, I.; Chapman, H. N.; Chen, C.; Cohen, B. E.; Conceição, A. L. C.; Cormode, D. P.; Cui, D.; Dawson, K. A.; Falkenberg, G.; Fan, C.; Feliu, N.; Gao, M.; Gargioni, E.; Glüer, C.-C.; Grüner, F.; Hassan, M.; Hu, Y.; Huang, Y.; Huber, S.; Huse, N.; Kang, Y.; Khademhosseini, A.; Keller, T. F.; Körnig, C.; Kotov, N. A.; Koziej, D.; Liang, X.-J.; Liu, B.; Liu, S.; Liu, Y.; Liu, Z.; Liz-Marzán, L. M.; Ma, X.; Machicote, A.; Maison, W.; Mancuso, A. P.; Megahed, S.; Nickel, B.; Otto, F.; Palencia, C.; Pascarelli, S.; Pearson, A.; Peñate-Medina, O.; Qi, B.; Rädler, J.; Richardson, J. J.; Rosenhahn, A.; Rothkamm, K.; Rübhausen, M.; Sanyal, M. K.; Schaak, R. E.; Schlemmer, H.-P.; Schmidt, M.; Schmutzler, O.; Schotten, T.; Schulz, F.; Sood, A. K.; Spiers, K. M.; Staufer, T.; Stemer, D. M.; Stierle, A.; Sun, X.; Tsakanova, G.; Weiss, P. S.; Weller, H.; Westermeier, F.; Xu, M.; Yan, H.; Zeng, Y.; Zhao, Y.; Zhao, Y.; Zhu, D.; Zhu, Y.; Parak, W. J., X-Ray-Based Techniques to Study the Nano–Bio Interface. *ACS Nano* **2021,** *15*, 3754-3807.
34. Alexander V. Naumkin, A. K.-V., Stephen W. Gaarenstroom, and Cedric J. Powell, Nist X-Ray Photoelectron Spectroscopy Database, Nist Standard Reference Database Number 20, National Institute of Standards and Technology, Gaithersburg Md, 20899 (2000). NIST, Ed. 2012.

35. Mohtasebi, A.; Chowdhury, T.; Hsu, L. H. H.; Biesinger, M. C.; Kruse, P., Interfacial Charge Transfer between Phenyl-Capped Aniline Tetramer Films and Iron Oxide Surfaces. *J. Phys. Chem. C* **2016,** *120*, 29248-29263.
36. Beamson, G.; Briggs, D. R. In *High Resolution Xps of Organic Polymers: The Scienta Esca300 Database*, 1992.
37. Molina-Reyes, J.; Tiznado, H.; Soto, G.; Vargas-Bautista, M.; Dominguez, D.; Murillo, E.; Sweeney, D.; Read, J., Physical and Electrical Characterization of Yttrium-Stabilized Zirconia (Ysz) Thin Films Deposited by Sputtering and Atomic-Layer Deposition. *J. Mater. Sci. - Mater. Electron.* **2018,** *29*, 15349-15357.
38. Jeon, Y.; Lee, C.; Lee, G.; Kwon, O.; Kim, J.; Park, S. S.; Oh, K.; Shul, Y.-G., Thermally Stable Imidazole/Heteropoly Acid Composite as a Heterogeneous Catalyst for M-Xylene Ammoxidation. *Res. Chem. Intermed.* **2021,** *47*, 287-302.
39. Ling, D.; Gao, L.; Wang, J.; Shokouhimehr, M.; Liu, J.; Yu, Y.; Hackett, M. J.; So, P. K.; Zheng, B.; Yao, Z.; Xia, J.; Hyeon, T., A General Strategy for Site-Directed Enzyme Immobilization by Using Nio Nanoparticle Decorated Mesoporous Silica. *Chem. Eur. J.* **2014,** *20*, 7916-21.
40. Bolivar, J. M.; Hidalgo, A.; Sanchez-Ruiloba, L.; Berenguer, J.; Guisan, J. M.; Lopez-Gallego, F., Modulation of the Distribution of Small Proteins within Porous Matrixes by Smart-Control of the Immobilization Rate. *J. Biotechnol.* **2011,** *155*, 412-20.
41. Rocha-Martín, J.; Rivas, B. d. l.; Muñoz, R.; Guisán, J. M.; López-Gallego, F., Rational Co-Immobilization of Bi-Enzyme Cascades on Porous Supports and Their Applications in Bio-Redox Reactions with in Situ Recycling of Soluble Cofactors. *ChemCatChem* **2012,** *4*, 1279-1288.
42. Grajales, D.; Mateos, J. C.; Padro, D.; Ramos-Cabrer, P.; López-Gallego, F., In-Flow Protein Immobilization Monitored by Magnetic Resonance Imaging. *N. Biotechnol.* **2018,** *47*, 25-30.
43. Logan, T. C.; Clark, D. S.; Stachowiak, T. B.; Svec, F.; Fréchet, J. M. J., Photopatterning Enzymes on Polymer Monoliths in Microfluidic Devices for Steady-State Kinetic Analysis and Spatially Separated Multi-Enzyme Reactions. *Anal. Chem.* **2007,** *79*, 6592-6598.
44. Santiago-Arcos, J.; Velasco-Lozano, S.; Diamanti, E.; Cortajarena, A. L.; López-Gallego, F., Immobilization Screening and Characterization of an Alcohol Dehydrogenase and Its Application to the Multi-Enzymatic Selective Oxidation of 1,-Omega-Diols. *Front. Catal.* **2021,** *1*, 9.
45. Velasco-Lozano, S.; Benítez-Mateos, A. I.; López-Gallego, F., Co-Immobilized Phosphorylated Cofactors and Enzymes as Self-Sufficient Heterogeneous Biocatalysts for Chemical Processes. *Angew. Chem. Int. Ed.* **2017,** *56*, 771-775.
46. Ji, X.; Su, Z.; Wang, P.; Ma, G.; Zhang, S., Tethering of Nicotinamide Adenine Dinucleotide inside Hollow Nanofibers for High-Yield Synthesis of Methanol from Carbon Dioxide Catalyzed by Coencapsulated Multienzymes. *ACS Nano* **2015,** *9*, 4600-4610.
47. Kim, H.; Rosa, C.; Boaro, M.; Vohs, J.; Gorte, R., Fabrication of Highly Porous Yttria Stabilized Zirconia by Acid Leaching Nickel from a Nickel–Yttria-Stablized Zirconia Cermet. *J. Am. Ceram. Soc.* **2002,** *85*, 1473-1476.
48. Bolte S; Cordelières, F. P., A Guided Tour into Subcellular Colocalization Analysis in Light Microscopy. *J. Microsc.* **2006,** *224*, 213-232.
49. Schindelin, J.; Arganda-Carreras, I.; Frise, E.; Kaynig, V.; Longair, M.; Pietzsch, T.; Preibisch, S.; Rueden, C.; Saalfeld, S.; Schmid, B.; Tinevez, J.-Y.;

White, D. J.; Hartenstein, V.; Eliceiri, K.; Tomancak, P.; Cardona, A., Fiji: An Open-Source Platform for Biological-Image Analysis. *Nat. Methods* **2012,** *9*, 676-682.
50. Gorlewicz, A.; Krawczyk, K.; Szczepankiewicz, A. A.; Trzaskoma, P.; Mulle, C.; Wilczynski, G. M., Colocalization Colormap –an Imagej Plugin for the Quantification and Visualization of Colocalized Signals. *Neuroinformatics* **2020,** *18*, 661-664.
51. Jaskolski, F.; Mulle, C.; Manzoni, O. J., An Automated Method to Quantify and Visualize Colocalized Fluorescent Signals. *J. Neurosci. Methods* **2005,** *146*, 42-9.